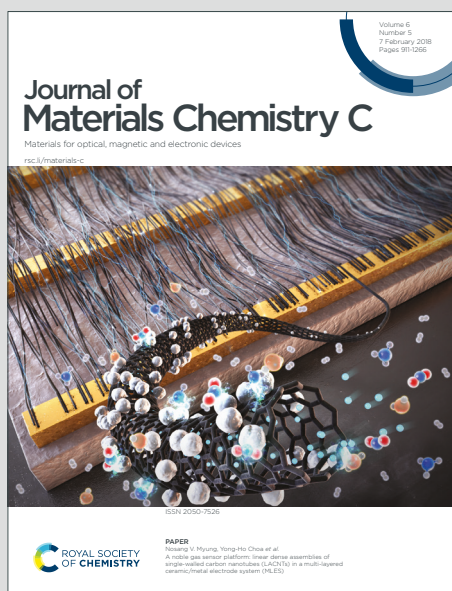


Journal of Materials Chemistry C

Materials for optical, magnetic and electronic devices

Accepted Manuscript

This article can be cited before page numbers have been issued, to do this please use: M. Pegu, S. Kazim, P. Huang, L. Lezama and S. Ahmad, *J. Mater. Chem. C*, 2021, DOI: 10.1039/D1TC01258D.



This is an Accepted Manuscript, which has been through the Royal Society of Chemistry peer review process and has been accepted for publication.

Accepted Manuscripts are published online shortly after acceptance, before technical editing, formatting and proof reading. Using this free service, authors can make their results available to the community, in citable form, before we publish the edited article. We will replace this Accepted Manuscript with the edited and formatted Advance Article as soon as it is available.

You can find more information about Accepted Manuscripts in the [Information for Authors](#).

Please note that technical editing may introduce minor changes to the text and/or graphics, which may alter content. The journal's standard [Terms & Conditions](#) and the [Ethical guidelines](#) still apply. In no event shall the Royal Society of Chemistry be held responsible for any errors or omissions in this Accepted Manuscript or any consequences arising from the use of any information it contains.

ARTICLE

Tetra-indole core as a dual agent: hole selective layer and for defect passivation in perovskite solar cellsMeenakshi Pegu,^a Samrana Kazim,^{a,c} Peng Huang,^a Luis Lezama,^b and Shahzada Ahmad^{a,c,*}Received 00th January 20xx,
Accepted 00th January 20xx

DOI: 10.1039/x0xx00000x

Organic small molecule composed of tetra-indole core was designed and introduced as hole selective layer for perovskite solar cells (PSCs) fabrication. 5,10,15,20-tetrahydrotriindole[2',3':4:2',3':5,6:2',3':7,8]cycloocta[1,2-b]indole (TTI) when integrated in PSCs, also passivate the defects in perovskite by suppressing the non-radiative recombination as noted from photoluminescence and electrochemical impedance (EIS) measurements and gave improve photovoltaic performances. The device showed a power conversion efficiency of 15.83% when employed as an HTM, however on passivating the interface of perovskite/HTL, the PCE improved significantly to 19.23%. Additionally, the TTI treated device showed improved charge transfer behaviour and long-term stability when store in dark under ambient atmosphere.

Introduction

Perovskite solar cells (PSCs) have attracted a surge of attention due to their outstanding performances in the thin film photovoltaic (PV) family. Its merits of being solution processable, intriguing photophysical properties, long carrier diffusion length, small exciton binding energy, led to rapid advances in power conversion efficiencies (PCE) through device engineering.¹⁻⁵ The certified PCE in excess of over 25.5% has put PSCs on par with well-established PV technologies and viable alternative to silicon-based as next-generation PV technology.⁶ The notable advancement in PV performances stems from device architecture, modulating the perovskite composition, growth of high quality perovskite and choice of charge extraction materials.⁷ To further boost the performances and reliability in PSCs, not only the development in active layer is required but also rational interfacial layers such as the hole transport layers and the electron transport layers is essential research.^{8,9}

The device architecture of PSCs is divided mainly into three classes: mesoporous, or planar (*n-i-p*) and inverted planar (*p-i-n*) structure.^{10,11} Currently, the most efficient PSCs are mainly based on *n-i-p* architect, where *n*-type layer of TiO₂/SnO₂ and *p*-type layer of Spiro-OMeTAD/PTAA are used, together with mixed halide perovskite as light absorbers.^{12,13} The hole transport materials (HTM) plays a critical role in PSCs not only to enhance the PCE but it also controls the stability of the PSCs by preventing moisture permeability into the perovskite layer. HTMs should possess higher hole conductivity and electron blocking properties.^{14,15} Numerous HTMs have been developed for PSC applications based on small molecules, polymers and inorganic materials.¹⁶ Inorganic HTMs are promising candidate

due to its high stability, however the PCE performance is limited by their surface defects, low intrinsic conductivity, poor solubility in common organic solvents and particle size reproducibility.¹⁷ Whereas, the polymers based HTM display decent morphological properties but low stability and reproducibility, especially when the dopants are used.¹⁸ Compared to the inorganic and polymeric counterparts, small molecules as HTM are viable alternatives owing to high purity and solubility, define molecular structure and good reproducibility. In addition, the interface properties between the perovskite and HTM plays a trivial role in achieving high reliability in PSCs.¹⁹⁻²² The interfacial property is dependent on the HTM layer, mainly due to their appropriate highest occupied molecular orbitals (HOMO) energy level for band alignment.²³ Spiro-OMeTAD is being considered as standard and is widely used HTM in PSCs. Spiro-OMeTAD induce instability in the PSCs on addition of the hygroscopic dopants, which is a prerequisite, as pristine Spiro-OMeTAD does not possess the intrinsic charge carrier mobility and the post-oxidation of the HTM has an adverse effect on the perovskite layer.²⁴ Besides, the high material cost, stemmed from multi-step synthesis process escalate the cost of PSCs.²⁵

Aromatic hydrocarbon are extensively studied class of materials owing to their unique electro-optical behaviour.²⁶⁻²⁸ Such molecules find applications in organic electronics such as organic field effect transistors (OFETS), organic light emitting diodes (OLEDs) and organic photovoltaics (OPVs). The development of new heterocyclic aromatic hydrocarbons with large π -extended systems as functional materials in organic electronics is being studied. Among the heterocycles, the indole based motifs are key heteroatomic molecules²⁹⁻³¹ as an HTM, light harvesters or emitters in the optoelectronic field, owing to its electrical and thermal merits.^{32,33} Among the various indole motifs, 10,15-dihydro-5H-diindolo[3,2-a:3',2'-c] carbazole (triindole or triazatruxene or TAT) was largely explored for PV applications. Since the seminal report of triazatruxene,³⁴

^a BCMaterials, Basque Center for Materials, Applications and Nanostructures, UPV/EHU Science Park, 48940, Leioa, Spain

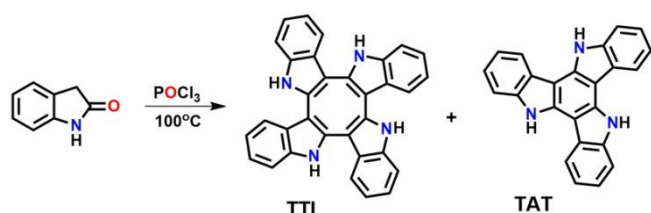
^b Email: shahzada.ahmad@bcmaterials.net

^c Departamento de Química Inorgánica, Facultad de Ciencia y Tecnología, Universidad del País Vasco, UPV/EHU, Sarriena s/n, 48940 Leioa, Spain

^d IKERBASQUE, Basque Foundation for Science, Bilbao, 48009, Spain

synthetic method from 2-indolone,³⁵ other TAT based derivatives were widely utilized as organic semiconductors in various optoelectronic field. Due to its easy modification of photophysical and electrochemical properties with strong π - π stacking and charge transport ability, indole motifs have been extensively studied.³⁶⁻³⁹ Additionally, the nitrogen atoms of indole moiety provides stability against oxidative doping from the atmospheric oxygen. Triazatruxene compound, constituting of two or more indole units, fused with six membered benzene rings with extended delocalized π -system was reported.⁴⁰ It is composed of three indole rings linked to central phenyl ring with extended π -system. The triindole based moiety allows structural substitution and modification to tune the optoelectrical properties.⁴¹

Similarly, cyclooctatetraene (COT) is another class of polycyclic aromatic compounds with a nonplanar saddle-shaped geometry consisting of 8- π annulene as the structure.^{42, 43}



Scheme 1: Synthesis of TTI and TAT.

The advantageous property of COT-based system includes the structural coalescing with aromatics systems such as phenyl, thiophene, furan, pyrimidine and thiazole.⁴⁰ Cyclic tetramer COT fused indole motif 5,10,15,20-tetrahydrotriindole[2',3':4:2',3':5,6:2',3':7,8]cycloocta[1,2-b]indole (TTI) was synthesized,^{44, 45} however it remains largely unexplored.

Result and Discussion

The molecular structure and synthesis route of TTI is shown in Scheme 1. Synthesis of the tetra-indole moiety was carried out in POCl_3 under dry environment in a single step. However, the reaction of 2-oxindole in POCl_3 provides both tri-indole and tetra-indole as the products.⁴⁰ Both the product mixtures were purified and the tetra-indole compound was characterized by NMR (^1H and ^{13}C) spectrometric analysis (Figure S1-S2). The ^1H and ^{13}C spectral pattern and relative integrated values are consistent with the structure of TTI. TTI was readily soluble in dichloromethane (DCM), tetrahydrofuran (THF) and partially in toluene. We measured the absorption of TTI in chlorobenzene, ethyl acetate and binary mixture of chlorobenzene and ethyl acetate (Figure 1a). The absorption spectra in the solvents show a clear π - π^* transition peak at 312.8 nm. However, the absorption peak in the spectra remains unaltered, indicating no intermolecular rotation in different solvent polarity for TTI.

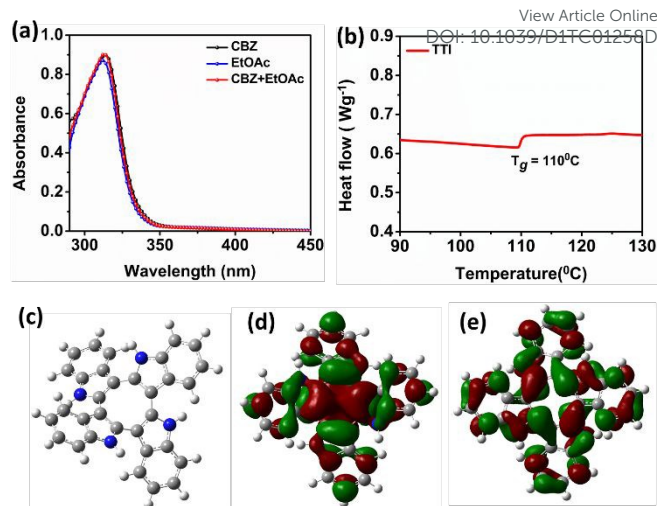


Figure 1: a) UV-Vis absorption spectra of TTI in various solvents. b) DSC traces of TTI under N_2 at a scanning rate of 10°C , c) optimized molecular conformation, d) HOMO and (e) LUMO of TTI calculated using Gaussian (B3LYP/631G (d)).

We measured the differential scanning calorimetry (DSC) profile, and TTI revealed a glass transition temperature (T_g) at 110°C (Figure 1b). We can expect that the tetra-indole moiety would offer a thermal and morphological stability during the PSCs fabrication and operation. No distinctive transitions for crystallization and melting behaviour during the DSC scan from the room temperature to 350°C was noted.

We run the density functional theory (DFT) calculation to ascertain the electronic transition in TTI,⁴⁰ and noted the highest occupied molecular orbital (HOMO) of -4.6 eV and the lowest unoccupied molecular orbital (LUMO) of -1.06 eV. The saddle shaped core of the tetra-indole derivative showed a twisted molecular structure (Figure 1c), with a non-planarity because of strong steric hindrance. The HOMO and LUMO of TTI was delocalized and loaded over the backbone of TTI (Figure 1d,e). Overlap of the partial wave function between the two orbitals was noted, which indicates that the delocalization occurs at the tetra-indole core and this can be beneficial for the neutral exciton generation and hole transfer transitions. Energetic level suggests TTI suitability as HTM for PSCs and further derivatization or doping of TTI can allow energy levels tuning.

Hole mobility was measured by fabricating a hole only device with the structure of FTO/PEDOT:PSS/HTM/Au. The hole mobility of TTI was measured using space charge limit current model. By fitting the current density-voltage (J - V) curve, we derived the mobility value according to the Mott-Gurney equation (Figure S3a). The undoped TTI showed higher mobility ($4.4 \times 10^{-5} \text{ cm}^2\text{V}^{-1}\text{s}^{-1}$) than of Spiro-OMeTAD ($5.1 \times 10^{-5} \text{ cm}^2\text{V}^{-1}\text{s}^{-1}$). While in the doped state, the mobility of Spiro-OMeTAD ($1.4 \times 10^{-4} \text{ cm}^2 \text{V}^{-1} \text{ s}^{-1}$) was higher than of TTI ($1.0 \times 10^{-5} \text{ cm}^2 \text{V}^{-1} \text{ s}^{-1}$). We measured the conductivity in a sandwich configuration (FTO/HTM/Au). The conductivity of the undoped TTI was found to be $1.21 \times 10^{-6} \text{ Scm}^{-1}$ and for the Spiro-OMeTAD was $0.318 \times 10^{-6} \text{ Scm}^{-1}$ (Figure S3b).

EPR spectroscopy experiments were designed to quantify the charge formation by doping and the mobility of the free radical

cations. The EPR measurements were carried out on similar conditions with a concentration of 30 mM solutions of doped and undoped Spiro-OMeTAD and TTI (Figure 2a).

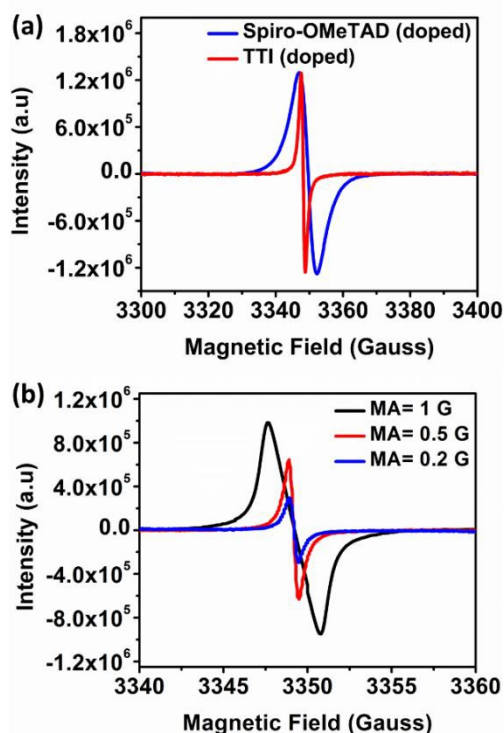


Figure 2: a) EPR spectra registered with 30mM chlorobenzene solutions of doped Spiro-OMeTAD and TTI, and b) influence of the modulation amplitude of the applied field on the EPR signal of doped TTI.

The undoped Spiro-OMeTAD solution shows the characteristics weak signal due to Spiro-OMeTAD⁺ species generated by natural oxidation.⁴⁶⁻⁴⁸ In all the cases, the intensity of the signals increases over time under illumination (Figure S4). However, the intensity of the signal gradually decreases after 24 hrs. With light exposure, a remarkable enhancement of the EPR signal was noted for the doped materials as compared to the undoped ones.

The spectral parameters were deduced by a computer simulation program working at the second order of the perturbation theory (Table S1). For all the samples good fits were obtained considering the presence of only a type of free radicals. Therefore, the photo-generated radicals appear to be similar to those derived from exposure to oxygen or oxidation by the dopants, but the photo-generation of radicals with very short lifetime ($<10^{-6}$ s) cannot be disregarded.⁴⁹ The values of the g -factor are not affected by the doping and are slightly higher for TTI samples indicating a higher orbital contribution, which implies that the unpaired electron resides longer on the nitrogen atoms. However, the most significant differences between both types of compounds are observed in the peak-to-peak linewidths. The signals observed for doped TTI is narrower than that of undoped or for the Spiro-OMeTAD solutions (c.a.

0.5 vs 5 Gauss). To detect the signal without distorting it, it was necessary to reduce the modulation amplitude of the EPR experiment to 0.2 G (Figure 2b).

In this type of free radicals' solutions, the linewidth of the EPR signal is mainly related to the density of the solvent (molecular movements), the concentration of the paramagnetic effects (exchange/dipolar intermolecular interactions) and the mobility of the spins. The peak-to-peak linewidth of the undoped Spiro-OMeTAD is 6.1 G, while 4.7 G for the doped sample. Similar peak narrowing of the peak for Spiro-OMeTAD doped samples after light irradiation was reported, and was attributed to the exchange narrowing derived from the increase of radical concentrations caused by both the irradiation and the dopants.⁵⁰ However, radical peak narrowing similar to the doped TTI was only observed for a Spiro:LiTFSi:*t-BP* after 40 days of light exposure. This narrowing of peak accompanied by a change from Lorentzian to Gaussian profile of the EPR lines in perovskite-Spiro-OMeTAD films was attributed to the formation of mobile holes by the light irradiation.⁵¹ In the present case, the concentration of spins is higher in the doped Spiro-OMeTAD than of doped TTI solution, therefore the narrowing of the signal cannot be attributed only to a fast intermolecular exchange. In addition, the fit of the doped TTI EPR signal has been achieved with a 100% Lorentzian line shape. Arguably, the doping of TTI favors the formation of mobile holes under light exposure.

The photon absorption of the perovskite with HTMs shows similar profile (Figure 3a). To investigate the charge extraction behaviour at the perovskite/HTM interface, the steady state PL spectra of the perovskites were recorded (Figure 3b). We noted significantly reformed in the PL peak of the perovskite (on the quartz) at 770 nm, after coating of TTI, and quenching display similar profile as of Spiro-OMeTAD. This discrepancy can be ascribed to the higher valence band (E_{HOMO}) of TTI as compared to Spiro-OMeTAD.

Table 1: Photovoltaic parameters of the TTI based fabricated PSCs

	V_{oc} (mV)	J_{sc} (mA/cm ²)	FF (%)	PCE (%)	R_s (Ω)	R_{shunt} (Ω)
PSK/HTM						
PSK/Spiro	1014	22.53	75.37	17.22	54.14	8522
PSK/TTI	1003	20.83	75.72	15.83	42.28	4353

The cross-sectional SEM image of the TTI based PSC (Figure 3c), shows the perovskite thickness between 450-500 nm and that of 30 mM TTI had a thickness of 73 nm. The microstructure of TTI with the perovskite (Figure S5), suggests smooth surface that can enhance the interfacial contact between perovskite and hole transporting layer.

To evaluate TTI as a potential core for HTM in PSCs we fabricated MAPbI₃ based devices in both *n-i-p* configuration {FTO/bl-mesoTiO₂/CH₃NH₃PbI₃/HTM/Au} and *p-i-n* configuration {FTO/HTM/CH₃NH₃PbI₃/PCBM/BAP/Au}.

ARTICLE

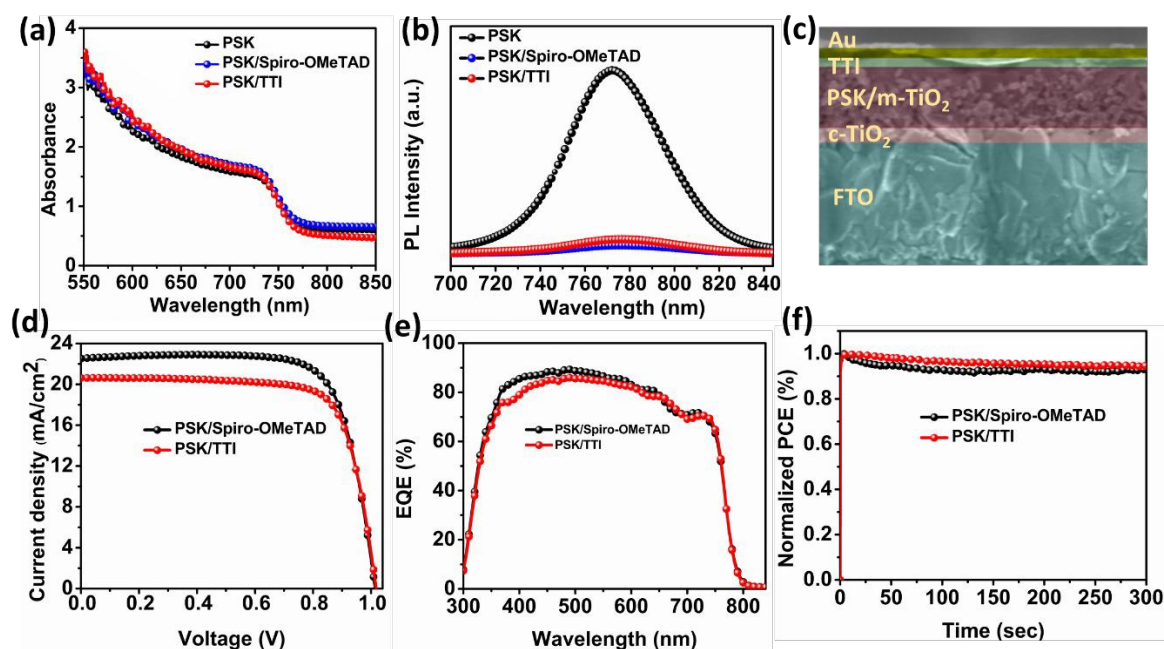


Figure 2: a) UV-Vis absorption spectra, b) Steady state PL spectra of perovskite and perovskite/HTM treated films, c) cross sectional SEM-image of the TTI based HTM fabricated device, d) current-voltage (J - V curves) characteristics of PSCs based on TTI and Spiro-OMeTAD, e) corresponding EQE spectra and f) the stabilized power output of the TTI and Spiro-OMeATD based PSCs.

The current density-voltage (J - V) curves for the n - i - p based PSCs under the illumination of 100 mWcm^{-2} AM 1.5G (Figure 3d), while the corresponding PV parameters the short circuit current (J_{sc}), open circuit voltage (V_{oc}), fill factor, and PCE are listed in Table 1. The PSCs fabricated with TTI exhibited a PCE of 15.8%. ($J_{sc} = 20.82 \text{ mAcm}^{-2}$, $V_{oc} = 1003 \text{ mV}$, $FF = 75.72\%$) with negligible hysteresis, while under similar condition, the Spiro-OMeTAD based PSC yielded a PCE of 17.22% ($J_{sc} = 22.53 \text{ mAcm}^{-2}$, $V_{oc} = 1.014 \text{ V}$, $FF = 75.37\%$). The device with TTI possessed similar V_{oc} and comparable FF values but lower J_{sc} values as compared to the standard Spiro-OMeTAD. We ascribed the marginally lower performance to the mismatch energy level as well as rate of charge extraction arises from lower mobility. The HOMO (as calculated from DFT) of TTI is lower as compared to Spiro-OMeTAD, resulting in lower open circuit voltage and lower short circuit current could ascribe to low hole mobility of doped TTI.

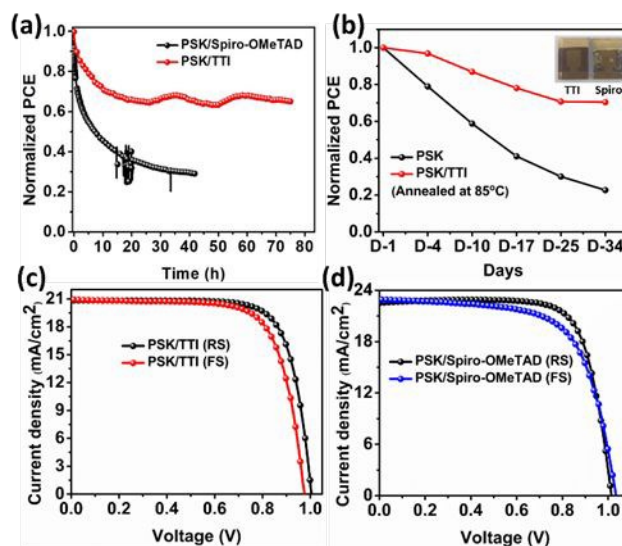


Figure 4: a) Maximum power point tracking for the PSK and PSK/TTI HTM without encapsulation for 1000 mins under 1 sun illumination at ambient condition, b) normalized PCE of the pristine and PSK/TTI HTM based PSCs under continuous annealing at 85°C at ambient atmospheric condition, c) current-voltage (J - V curves) characteristics of forward and reverse scans of PSCs based on TTI, and d) with Spiro-OMeTAD, under Air-Mass (AM) 1.5G illumination.

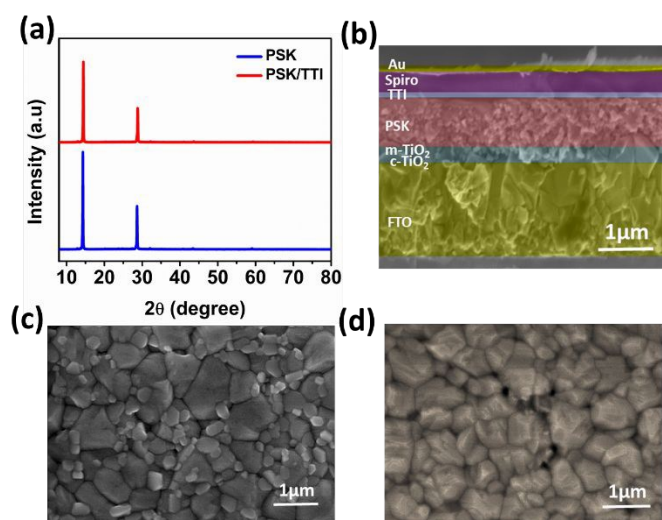


Figure 5: a) X-ray diffraction patterns of the pure PSK and TTI treated thin films, b) cross sectional SEM-image of the 3 mg/mL TTI treated device; surface SEM images of, c) pure perovskites and d) TTI treated perovskites.

The series resistance and shunt resistance for TTI based PSC showed a value of 42.28 Ω and 43.53 k Ω whereas the Spiro-OMeTAD the derived value was 54.14 Ω and 85.22 k Ω . The statistics of fabricated PSCs with TTI exhibited a PCE of 15.13%, which is slightly lower than that of the PSC with Spiro-OMeTAD under the similar conditions. The corresponding external quantum efficiency (EQE) was recorded (Figure 3e) and illustrates photon to current response covering the broad spectrum from 300 – 800 nm. An onset of photocurrent

generation is displayed in the EQE spectra, which is in congruence with the band gap of the perovskite. Expectedly, the device with TTI exhibits slightly lower EQE than that of Spiro-OMeTAD due to lower J_{sc} value obtained. We measured the steady state output of TTI and Spiro-based PSCs for period of time (300 s) and the TTI based PSCs showed higher reliability as compared to the Spiro-OMeTAD (Figure 3f).

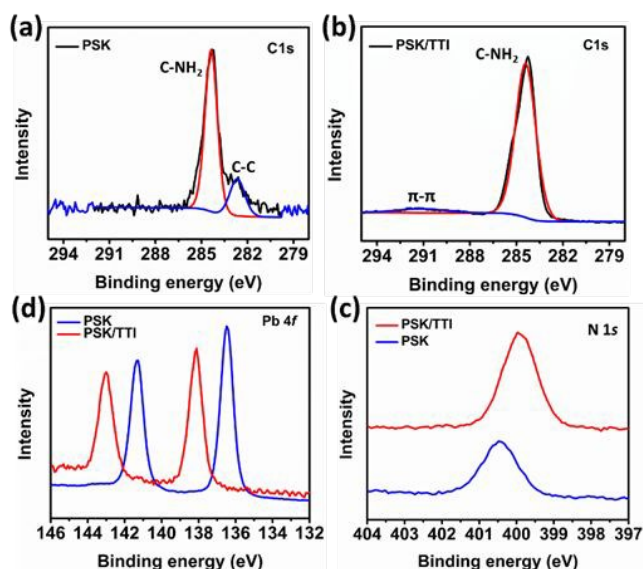


Figure 6: a,b) X-ray photoelectron spectroscopy (XPS), high resolution deconvoluted spectra of C1s, c) Pb 4f and d) N 1s, peaks of the PSK and TTI passivated perovskite.

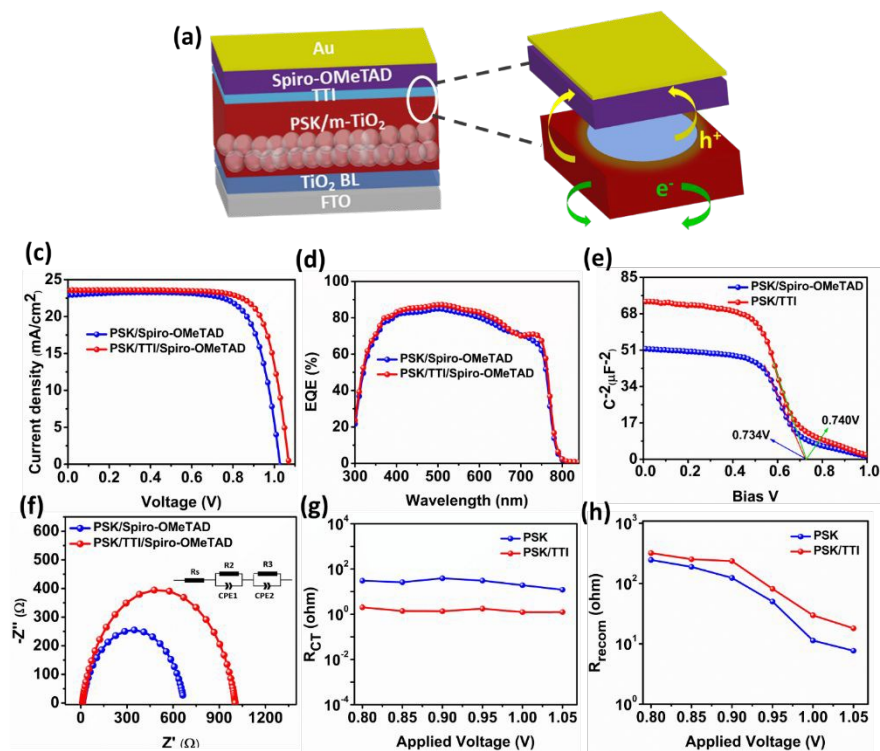


Figure 7: a) Device architecture of TTI treated PSCs, b) band alignment diagram of TTI passivated PSCs, c) current-voltage (J - V curves) of PSCs, d) corresponding EQE spectra, e) Mott Schottky plot, f) Nyquist plots for PSCs with and without TTI passivation, g) charge transfer resistance at applied voltage for PSK and PSK/TTI passivation, and h) recombination resistance at applied voltage PSK and PSK/TTI passivated PSC.

ARTICLE

Moreover, we further evaluated the long-term moisture and thermal stability of the PSCs (Figure 4a, b). It can be deduced from the figure, 70 % of its initial PCE was retained for the TTI based un-encapsulated device, kept at room temperature with a relative humidity of 50-60%. Furthermore, we noted nearly 80% of its initial PCE value retention for TTI based PSCs upon thermal annealing at 85°C, demonstrating its superior thermal stability. Notably, only 30mM of TTI was employed as compared to 70mM of Spiro-OMeTAD, this will further cut down the materials consumption and reduce the cost.

The hysteresis index (HI) was calculated by measuring the devices in both the forward scan (FS) and reverse scan (RS) direction (Figure 4c, d). TTI based PSCs showed low HI of 0.060 compared to Spiro-OMeTAD (0.084). The HI of the devices was calculated according to the equation:

$$HI = [J_{RS}(0.8 V_{oc}) - J_{FS}(0.8 V_{oc})] / J_{RS}(0.8 V_{oc})$$

We believe that with further derivatization of TTI at different -NH position and coupling will allow it to be an efficient and cost effective HTM. We also fabricated inverted PSCs with TTI as HTM in a device architecture FTO/TTI/CH₃NH₃PbI₃/PCBM/BCP/Ag (Figure S6). The PCE of the inverted PSCs with TTI exhibits 10.48% (V_{oc} = 825 mV, J_{sc} = 23.43 mA/cm² and FF = 54.19%).

Arguably, the four -NH group with the electron pairs in the tetra-indole core of TTI can also act as Lewis bases and expectedly passivate the positively charge defects and trap states of the perovskite layer.⁵² The strong electron donating ability of the -NH group in TTI can help in coordinating with the Pb²⁺, leading to Lewis-adduct formation, that can deactivate the positively charged defects on the surface of the perovskite layer.

Table 2: Photovoltaic parameters of the fabricated passivated PSCs

PSK/HTM	V_{oc} (mV)	J_{sc} (mA/cm ²)	FF (%)	PCE (%)	R_s (Ω)	R_{shunt} (Ω)
PSK/Spiro	1027	22.90	74.92	17.64	53.84	8330
PSK/TTI/Spiro	1070	23.55	76.29	19.23	46.74	121755

The placement of the interfacial layer can also be advantageous in improving the charge extraction by the interface and readily lowering the non-radiative recombination in the PSCs.⁵³ Crystallinity of the perovskite upon the passivation by TTI was analysed by X-ray diffraction (XRD) measurement. We noted the diffraction peaks at 14.28°, 28.65° is related to the (110) and (220) planes of the perovskite crystal (Figure 5a). XRD peaks intensity after TTI treatment tends to decrease slightly; plausibly due to the amorphous nature of the TTI passivated

layer atop the perovskite, that suppress the peak signal and bury the intensity.

The PV performance of the fabricated PSCs improved on treatment with TTI at the interface between perovskite and the hole selective layer. We fabricated the PSCs in *n-i-p* configuration: FTO/bl-mesoTiO₂/PSK/TTI/Spiro-OMeTAD. The cross-sectional SEM image of the TTI treated device, along with the surface images of perovskite layer with and without TTI treatment are presented (Figure 5b-d).

To decipher the coordination between TTI and perovskite, we performed X-ray photoelectron spectroscopy (XPS). The core level peak of C1s spectra shows the presence of TTI on the surface of the perovskite layer (Figure 6a, b).⁵⁴ The binding energy of Pb core electrons in Pb 4f_{7/2} and Pb 4f_{5/2} was shifted by 1.7 eV towards higher ionization potentials (Figure 6c), which experimentally ascribes the formation of covalent bond between TTI and Pb atoms in the perovskite. Moreover, N 1s peak shifting and increase in number of N atoms in the TTI treated perovskites, indicates the increment in electron cloud density of the lone pairs of N-atoms interacting with the Pb²⁺ ions of the perovskite. The I 3d peak of the TTI treated perovskite (Figure S7), shows the different binding energies of the organic structure on the surface of the perovskite.

The adopted PSCs architecture, substantiates the effective transport of charges (Figure 7a), and the band alignment of TTI with respect to perovskite (Figure 7b). The *J-V* curves upon TTI passivation (Figure 7c) shows improvement in the PCE. The PSCs with MAPbI₃ showed initial PCE of 17.64% (V_{oc} = 1027 mV, J_{sc} = 22.90 mA/cm², FF = 74.92%) while a superior PCE of 19.23% (V_{oc} = 1070 mV, J_{sc} = 23.55 mA/cm², FF = 76.29%) was measured upon TTI treatment (Table 2). The series resistance (R_s) and shunt resistance (R_{sh}) were extracted from the *J-V* curves, while the R_s values are nearly similar, R_{sh} was increased intensely for the TTI treated PSCs. This further ascribes the suppression of shunting current pathway upon TTI passivation. We calculated the hysteresis index (HI) (Figure S8), for pristine PSCs (0.176) and the HI value reduces to 0.07 for TTI passivated PSCs. The reduced HI suggests reduction in traps-state density of the perovskite with TTI passivation. From the PSCs statistics, it is evident that the average values of the PV parameters improved upon TTI passivation (Figure S9). The average V_{oc} increases from 1020± 9.3 mV to 1070± 10 mV, which is attributed to the decreased non-radiative recombination and enhanced charge carrier lifetime. The average FF improved from 75±4.26 to 76±1.58 due to improved hole extraction and reduced density of traps. Similarly, the overall PCE was improved from 17.64±1.12 to 19.23±0.42 with TTI passivated PSCs. In the EQE for the TTI treated and pristine PSCs (Figure 7d), an onset of photocurrent generation was noted which is in congruence with

the band gap of the perovskite. In the whole spectrum region, the PSCs with TTI passivation exhibits an improved EQE.

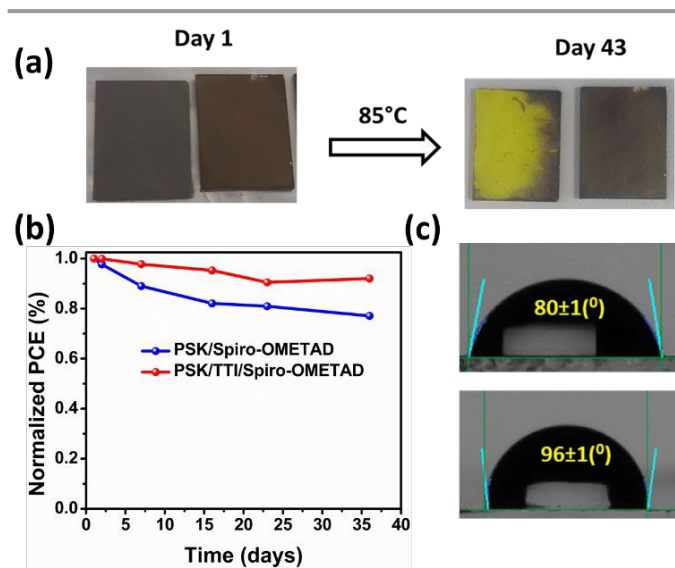


Figure 8: (a) Thin films of PSK (top left; both sides) and PSK/TTI (top right; both sides) under thermal annealing and ageing at 85°C at ambient atmospheric conditions (b) Comparison of device stability with and without TTI treatment and (c) contact angle measurements pure perovskites (top) and TTI treated (bottom) films.

The photo-carrier density increases in the photoactive layer in case of reduced non-radiative charge recombination. The quasi-Fermi-level splitting, in this case, is enhanced, which thereby increases the build-in-potential (V_{bi}) of the PSCs and subsequently, gives improved PCE. We measured the Mott Schottky plot made under dark condition (Figure 7e) for pristine and TTI passivated PSCs. The build-in potential (V_{bi}) and depletion layer width (W) was derived from C^{-2} - V plot.^{55, 56} An improved build in potential of 740 mV for the TTI treated PSC was extracted, at 10 kHz, while the pristine PSC gave a value of 734 mV. The calculated V_{bi} value for TTI treated device is slightly higher as compared to the untreated one, which ascribes enhanced charge extraction and high photocurrent. Additionally, with the increase in the build in potential V_{bi} , we calculated the depletion width (W) for pristine PSC and the TTI passivated PSC ($W = \sqrt{((2\epsilon_0\epsilon_r oV_{bi})/qN)}$ where, ϵ_r is the dielectric constant, ϵ_0 is the permittivity of the vacuum, V_{bi} is the build in potential, N is the density of fully ionized defects). The depletion layer width (W) was calculated to be 168.51 nm for the pristine PSC, and this increases to 198.55 nm for TTI passivated PSCs

To further substantiate the passivation effects, the electrochemical impedance spectroscopic (EIS) analysis was performed (Figure 7f), and the spectral analysis provide insight in the charge transfer and recombination behavior.^{57, 58} The Nyquist plots was measured in the dark at 0.8V. We deduced that the recombination resistance in the TTI passivated PSC (larger semicircle) is higher as compared to the pristine PSCs, TTI passivation leads to larger recombination resistance and elucidate its role in passivating the defects.

The charge transfer resistance and recombination resistance as function of voltage (Figure 7g, h) was derived from Nyquist plots (Figure 7f, S10), which display a single arc and the used equivalent circuit model is shown. The profile of the recombination resistance follows similar trend and at voltage close to V_{oc} , they display lower recombination, suggesting the key contribution of recombination processes are in the bulk of the perovskite. With the passivation of TTI lower recombination resistance was noted, suggesting its use to suppress non-radiative recombination losses. Recombination resistance, near to the V_{oc} , is higher for TTI passivated PSCs, pointing a reduction in the non-radiative recombination defects. Furthermore, the charge transfer resistance was lower for TTI treated PSCs, which we ascribed to the filling of grain boundaries as well as defects passivation.

The passivation of the perovskite layer by TTI is expected to enhance the stability of the PSCs. We investigated the impact of thermal and atmospheric stability on perovskite and TTI passivated perovskite (Figure 8a). The optical absorbance spectra were recorded for the freshly prepared films with and without TTI treatment (Figure S11 a). The films were left for ageing under continuous heating at 85°C (ambient atmosphere) and the absorbance spectra was recorded accordingly (Figure S11 b, c). Our results indicate that the absorption onset of the TTI treated perovskite was similar and the dark color of the perovskite was also maintained, while the pristine perovskite shows degradation (yellow colored) upon continuous heating and exposure to the ambient atmospheric conditions. TTI passivated perovskite film showed excellent stability upon continuous exposure to relative humidity and heat. We studied the long-term stability and measured the PCE with and without TTI passivation, periodically (stored in a dry box 30-40% relative humidity at RT) for a period of 36 days. The PCE values of the PSCs with TTI maintained about 90% of initial values whereas the pristine PSCs retained only 77% of its initial values after 36 days (Figure 8b). The hydrophobicity induced by TTI can also be deduced by the contact angle measurement (Figure 8c), which showed higher angle of 96° for TTI treated as compared to the untreated one 80°, this will induce device stability.

Conclusions

A tetra-indole based core as small molecule was design and studied as hole transporting material. TTI gave competitive performance when used as hole selective layers in perovskite solar cells, furthermore, the photovoltaic performance was improved when used as passivating agent. A PCE of 19.23% was obtained when TTI was placed as an interfacial layer. Thermal admittance spectroscopy suggests that TTI helped in reducing the defects and reduction in the non-radiative recombination. Furthermore, the hydrophobic nature of TTI helped in enhancing the stability of the device. We believe that further derivatization of the TTI core will accelerate its investigation as effective hole transporting materials to rival the use of Spiro-OMETAD. Our approach suggests its dual functionality as hole transporting materials as well as substituting the use of organic

moieties and complementing to improve the defects in perovskite layer.

Experimental

Materials:

2-oxindole, POCl₃ were purchased from Alfa Aesar. Lead Iodide (99.9%) was procured from Tokyo Chemical Industry (TCI) and employed as such. Methyl ammonium Iodide (MAI) was purchased from Dyesol. Solvents DMF, DMSO, Ethyl acetate, Ethanol, Chlorobenzene were purchased from Acros Chemicals and used as such.

Synthesis of TTI

Solution of indoline-2-one (5g, 37.55 mmol) in POCl₃ (25 mL) was stirred and refluxed at 80°C for 8 hours. After cooling the mixture, it was slowly poured into ice water and stirred for 30 minutes. The mixture solution was slowly neutralized by adding KOH solution under continuous stirring. A dark green crude was obtained after extraction. The crude product was purified using silica gel column chromatography adding pure DCM to obtain TTI (16.27%) and TAT (18.1 %) as pale-yellow solids. ¹H NMR (500MHz, DMSO-d₆): δ ppm; 11.43 (s, 4H), 7.57 (d, J= 7.6, 4H), 7.41 (d, j=7.7, 4H), 7.07 (m, 8H); ¹³C (125 MHz, DMSO-d₆): δ ppm; 137.75, 135.23, 127.81, 121.73, 120.02, 119.17, 111.80, 105.99.

Device Fabrication

Fluorine doped tin oxide (FTO) coated glass (NSG11) was cleaned in sequence prior to use. Ultrasonication (2% Hellmanex water solution for 30 minutes) followed by rinsing with deionized water, acetone and then isopropanol (IPA). Finally, the electrodes were treated under UV-Ozone for 30 minutes for the removal for residual on the surface. TiO₂ compact layer was deposited on the cleaned FTO substrate via spray pyrolysis at 500 °C using a precursor solution of titanium diisopropoxide bis(acetylacetonate) in anhydrous ethanol (1:19). Post spray, the substrates were left at 500 °C for further 30 minutes and allowed to cool down. Mesoporous TiO₂ layer was deposited on these electrodes through spin coating process (30 s at 4000 rpm); for this, a TiO₂ paste (Dyesol 30 NR-D) was diluted to 1:8 in ethanol. The electrodes were annealed firstly at 125 °C, followed by 500 °C using programable ramp in a four-step heating and was then maintained at 500°C for 30 min to acquire anatase phase. On attaining room temperature, the substrates were treated under UV-Ozone for 30 minutes and transferred to an argon-filled glove-box for perovskite layer deposition. The precursor solution for preparing the MAPbI₃ was prepared by dissolving MAI (1.2 M) and PbI₂ (1.2 M) in DMSO. The perovskite solution was spin coated in a two-step sequence at 1000 and 4000 rpm for 10 s and 30 s, respectively. During the second step, 110 μL of chlorobenzene was dripped as an antisolvent approach on the substrate 5s prior the end of the spinning process. The perovskite coated substrates were annealed at 100 °C for 50 mins in a glovebox. On acquiring room temperature, the hole selective layer TTI (30mM) was deposited. Spiro-OMeTAD (70 mM) was prepared by dissolving the corresponding amount of materials in 1 mL chlorobenzene. The HTLs were doped by adding bis-(trifluoromethylsulfonyl)imide lithium salt (Li-TFSI) and 4-*tert*-Butylpyridine (*t*-BP) in the molar ratio 0.5 and 3.3 respectively. 40 μL of HTM solutions were spin-coated atop of the perovskite

layer at 4000 rpm for 30 s, in an argon filled glove box. For the passivation of MAPbI₃ layer, 3mg/mL TTI was dissolved and spin coated on top of the perovskite layer at 4000 rpm for 30 s and annealed at 100°C for 7 mins. The device was finished by evaporating Au layer of 75 nm as cathode under low vacuum (10⁻⁶ torr). All solutions were prepared inside an argon-filled glove box with controlled moisture and oxygen conditions (O₂ <10 ppm, H₂O < 2 ppm).

Device characterization

The device photovoltaics parameters were acquired by means of current density–voltage (*J*–*V*) curves, logged with a Keithley 2400 source-meter under AM 1.5 G, 100 mW cm² illumination from a 450 W AAA solar simulator (ORIEL, 94023 A). NREL certified monocrystalline silicon solar cell was used for calibration. A black metal mask (0.16 cm²) was used over the square size active area (0.5 cm²) to reduce the influence of scattered light. The devices were measured at a scan rate: 100 mV s⁻¹, pre-sweep delay: 10 s). The external quantum efficiency (EQE) measurements were carried out using a 150W Xenon lamp attached to with Bentham PVE300 motorized 1/4m monochromator as the light source.

Thin film Characterization

The surface microstructure with and without the passivation layer were examined by the scanning electron microscope (SEM). The thin films were prepared on quartz substrate by spin coating for structural characterization; the films were prepared by spin coating of MAPbI₃ and 3mg/mL TTI/PSK treatment. X-ray diffractograms were recorded using the D8 Advance diffractometer from Bruker (Bragg-Bretanto geometry, with an X-ray tube Cu Kα, λ=1.5406 angstrom). A scan of 5-10° was selected with an acquisition time of 1°/min. The absorption spectra were measured under UV-Vis-IR spectrophotometer (Varian Cary 50 UV/Vis Spectrophotometer). Photoluminescence (PL) steady state measurements were recorded with a spectrophotometer (Perkin Elmer Instrument LS55). XPS measurements were carried out on a SPECS system (Berlin, Germany) equipped with Phoibos 150 ID-DLD analyzer with monochromator Al Kα radiation (1486.7 eV).

Author CRediT

M.P. performed the experiments, analysed the data and prepared the initial draft, S.K. performed the electro-optical measurements, analysis of the data and suggested the idea, PH performed mobility experiments, L.L performed the EPR measurements and analysed the data and S.A. supervised & directed the research. All authors contributed to draft and prepared the final version.

Conflicts of interest

The authors declare no conflict of interest.

Acknowledgements

This work received funding from the European Union H2020 Programme under a European Research Council Consolidator grant [MOLEMAT, 726360]. We thank SGiKER, UPV-EHU for the NMR analysis.

Notes and references

1. A. Kojima, K. Teshima, Y. Shirai and T. Miyasaka, *J. Am. Chem. Soc.*, 2009, **131**, 6050-6051.
2. J. M. Ball, M. M. Lee, A. Hey and H. J. Snaith, *Energy Environ. Sci.*, 2013, **6**, 1739-1743.
3. N. J. Jeon, J. H. Noh, W. S. Yang, Y. C. Kim, S. Ryu, J. Seo and S. I. Seok, *Nature*, 2015, **517**, 476-480.
4. M. Grätzel, *Acc. Chem. Res.*, 2017, **50**, 487-491.
5. T. Zhou, M. Wang, Z. Zang, X. Tang and L. Fang, *Sol. Energy Mater. Sol. Cells*, 2019, **191**, 33-38.
6. *Best Research-Cell Efficiency Chart*, National Renewable Energy Laboratory (NREL); <https://www.nrel.gov/pv/cell-efficiency.html> (accessed 2021-04-26).
7. J. Y. Kim, J.-W. Lee, H. S. Jung, H. Shin and N.-G. Park, *Chem. Rev.*, 2020, **120**, 7867-7918.
8. A. K. Jena, A. Kulkarni and T. Miyasaka, *Chem. Rev.*, 2019, **119**, 3036-3103.
9. G. Xing, N. Mathews, S. Sun, S. S. Lim, Y. M. Lam, M. Grätzel, S. Mhaisalkar and T. C. Sum, *Science*, 2013, **342**, 344-347.
10. Y. Zhao and K. Zhu, *Chem. Soc. Rev.*, 2016, **45**, 655-689.
11. Z. Liu, A. Zhu, F. Cai, L. Tao, Y. Zhou, Z. Zhao, Q. Chen, Y.-B. Cheng and H. Zhou, *J. Mater. Chem. A*, 2017, **5**, 6597-6605.
12. L. Calió, S. Kazim, M. Grätzel and S. Ahmad, *Angew. Chem. Int. Ed.*, 2016, **55**, 14522-14545.
13. P. Huang, Manju, S. Kazim, G. Sivakumar, M. Salado, R. Misra and S. Ahmad, *ACS Appl. Mater. Interfaces*, 2020, **12**, 22881-22890.
14. K. Rakstys, C. Igci and M. K. Nazeeruddin, *Chem. Sci.*, 2019, **10**, 6748-6769.
15. N. J. Jeon, H. Na, E. H. Jung, T.-Y. Yang, Y. G. Lee, G. Kim, H.-W. Shin, S. I. Seok, J. Lee and J. Seo, *Nat. Energy*, 2018, **3**, 682-689.
16. J. Urieta-Mora, I. García-Benito, A. Molina-Ontoria and N. Martín, *Chem. Soc. Rev.*, 2018, **47**, 8541-8571.
17. S. S. Mali, J. V. Patil, J. A. Steele, S. R. Rondiya, N. Y. Dzade and C. K. Hong, *ACS Energy Lett.*, 2021, **6**, 778-788.
18. Q. Zhao, R. Wu, Z. Zhang, J. Xiong, Z. He, B. Fan, Z. Dai, B. Yang, X. Xue and P. Cai, *Org. Electron.*, 2019, **71**, 106-112.
19. M. Wang, H. Wang, W. Li, X. Hu, K. Sun and Z. Zang, *J. Mater. Chem. A*, 2019, **7**, 26421-26428.
20. M. Wang, W. Li, H. Wang, K. Yang, X. Hu, K. Sun, S. Lu and Z. Zang, *Adv. Electron. Mater.*, 2020, **6**, 2000604.
21. Z. Zhou, S. Pang, Z. Liu, H. Xu and G. Cui, *J. Mater. Chem. A* 2015, **3**, 19205-19217.
22. T. Zhou, M. Wang, Z. Zang and L. Fang, *Adv. Energy Mater.*, 2019, **9**, 1900664.
23. M. Hao, W. Chi and Z. Li, *Nanoscale*, 2021.
24. X. Yin, Z. Song, Z. Li and W. Tang, *Energy Environ. Sci.*, 2020, **13**, 4057-4086.
25. N. Li, X. Niu, Q. Chen and H. Zhou, *Chem. Soc. Rev.*, 2020.
26. P. T. Herwig and K. Müllen, *Adv. Mater.*, 1999, **11**, 480-483.
27. Y.-J. Cheng, S.-H. Yang and C.-S. Hsu, *Chem. Rev.*, 2009, **109**, 5868-5923.
28. S. Hashimoto, T. Ikuta, K. Shiren, S. Nakatsuka, J. Ni, M. Nakamura and T. Hatakeyama, *Chem. Mater.*, 2014, **26**, 6265-6271.
29. S. Wakim, J. Bouchard, M. Simard, N. Drolet, Y. Tao and M. Leclerc, *Chem. Mater.*, 2004, **16**, 4386-4388.
30. E. Wang, W. Mammo and M. R. Andersson, *Adv. Mater.*, 2014, **26**, 1801-1826.
31. N. Wahlström, J. Slätt, B. Stensland, A. Ertan, J. Bergman and T. Janosik, *J. Org. Chem.*, 2007, **72**, 5886-5889.
32. E. Wang, W. Mammo and M. R. Andersson, *Adv. Mater.*, 2014, **26**, 1801-1826.
33. L. Gao, T. H. Schloemer, F. Zhang, X. Chen, C. Xiao, K. Zhu and A. Sellinger, *ACS Appl. Energy Mater.*, 2020, **3**, 4492-4498.
34. J. Bergman and N. Eklund, *Tetrahedron*, 1980, **36**, 1445-1450.
35. M. A. Eissenstat, M. R. Bell, T. E. D'Ambra, E. J. Alexander, S. J. Daum, J. H. Ackerman, M. D. Gruett, V. Kumar and K. G. Estep, *J. Med. Chem.*, 1995, **38**, 3094-3105.
36. F. Wang, X.-C. Li, W.-Y. Lai, Y. Chen, W. Huang and F. Wudl, *Org. Lett.*, 2014, **16**, 2942-2945.
37. K. Rakstys, A. Abate, M. I. Dar, P. Gao, V. Jankauskas, G. n. Jacopin, E. Kamarauskas, S. Kazim, S. Ahmad and M. Grätzel, *J. Am. Chem. Soc.*, 2015, **137**, 16172-16178.
38. F. J. Ramos, K. Rakstys, S. Kazim, M. Grätzel, M. K. Nazeeruddin and S. Ahmad, *RSC Adv.*, 2015, **5**, 53426-53432.
39. L. Calió, C. Momblona, L. Gil-Escrig, S. Kazim, M. Sessolo, Á. Sastre-Santos, H. J. Bolink and S. Ahmad, *Sol. Energy Mater. Sol. Cells*, 2017, **163**, 237-241.
40. F. Wang, X.-C. Li, W.-Y. Lai, Y. Chen, W. Huang and F. Wudl, *Org. Lett.*, 2014, **16**, 2942-2945.
41. A. Connell, Z. Wang, Y.-H. Lin, P. C. Greenwood, A. A. Wiles, E. W. Jones, L. Furnell, R. Anthony, C. P. Kershaw and G. Cooke, *J. Mater. Chem. C*, 2019, **7**, 5235-5243.
42. A. Matsuura and K. Komatsu, *J. Am. Chem. Soc.*, 2001, **123**, 1768-1769.
43. H. Hiyoshi, T. Sonoda and S. Mataka, *Heterocycles*, 2006, **68**, 763-769.
44. O. Talaz and N. Saracoglu, *Tetrahedron*, 2010, **66**, 1902-1910.
45. M. Yurtsever and E. Yurtsever, *Polymer*, 2002, **43**, 6019-6025.
46. A. Abate, D. J. Hollman, J. I. Teuscher, S. Pathak, R. Avolio, G. D'Errico, G. Vitiello, S. Fantacci and H. J. Snaith, *J. Am. Chem. Soc.*, 2013, **135**, 13538-13548.
47. G. Sathiyam, A. A. Syed, C. Chen, C. Wu, L. Tao, X. Ding, Y. Miao, G. Li, M. Cheng and L. Ding, *Nano Energy*, 2020, **72**, 104673.
48. L.-L. Jiang, Z.-K. Wang, M. Li, C.-H. Li, P.-F. Fang and L.-S. Liao, *J. Mater. Chem. A* 2019, **7**, 3655-3663.
49. T. Nagamori and K. Marumoto, *Adv. Mater.*, 2013, **25**, 2362-2367.
50. F. Lamberti, T. Gatti, E. Cescon, R. Sorrentino, A. Rizzo, E. Menna, G. Meneghesso, M. Meneghetti, A. Petrozza and L. Franco, *Chem*, 2019, **5**, 1806-1817.
51. M. Namatame, M. Yabusaki, T. Watanabe, Y. Ogomi, S. Hayase and K. Marumoto, *Appl. Phys. Lett.*, 2017, **110**, 123904.
52. B. Chen, P. N. Rudd, S. Yang, Y. Yuan and J. Huang, *Chem. Soc. Rev.*, 2019, **48**, 3842-3867.
53. M. Salado, M. Andresini, P. Huang, M. T. Khan, F. Ciriaco, S. Kazim and S. Ahmad, *Adv. Funct. Mater.*, 2020, **30**, 1910561.
54. Q. Zhou, L. Liang, J. Hu, B. Cao, L. Yang, T. Wu, X. Li, B. Zhang and P. Gao, *Adv. Energy Mater.*, 2019, **9**, 1802595.
55. K. Jiang, J. Wang, F. Wu, Q. Xue, Q. Yao, J. Zhang, Y. Chen, G. Zhang, Z. Zhu and H. Yan, *Adv. Mater.*, 2020, **32**, 1908011.
56. M. Pegu, S. Kazim, T. Buffeteau, D. M. Bassani and S. Ahmad, *ACS Appl. Energy Mater.*, 2021, **4**, 3130-3140.
57. M. T. Khan, P. Huang, A. Almohammed, S. Kazim and S. Ahmad, *iScience*, 2021, **24**, 102024.
58. S.-Y. Wang, C.-P. Chen, C.-L. Chung, C.-W. Hsu, H.-L. Hsu, T.-H. Wu, J.-Y. Zhuang, C.-J. Chang, H. M. Chen and Y. J. Chang, *ACS Appl. Mater. Interfaces*, 2019, **11**, 40050-40061.

ARTICLE

Journal Name

View Article Online
DOI: 10.1039/D1TC01258D

Journal of Materials Chemistry C Accepted Manuscript

Published on 28 April 2021. Downloaded by RUTGERS STATE UNIVERSITY on 5/15/2021 8:31:04 PM.